


Artificial optoelectronic synapses based on Ga₂O₃ metal–semiconductor–metal solar-blind ultraviolet photodetectors with asymmetric electrodes for neuromorphic computing

Huazhen Sun¹ | Bingjie Ye¹ | Mei Ge² | Biao Gong¹ | Leyang Qian¹ |
Irina N. Parkhomenko³ | Fadei F. Komarov⁴ | Yu Liu⁵ | Guofeng Yang¹ 

¹School of Science, Jiangsu Provincial Research Center of Light Industrial Optoelectronic Engineering and Technology, Jiangnan University, Wuxi, Jiangsu, China

²School of Microelectronics, School of Integrated Circuits, Nantong University, Nantong, China

³Faculty of Radiophysics and Computer Sciences, Belarusian State University, Minsk, Belarus

⁴A.N. Sevchenko Institute of Applied Physical Problems of Belarusian State University, Minsk, Belarus

⁵Center for Quantum Devices, Niels Bohr Institute, University of Copenhagen, Copenhagen, Denmark

Correspondence

Guofeng Yang.

Email: gfyang@jiangnan.edu.cn

Abstract

Research on optoelectronic synapses that can integrate both detection and processing functions is essential for the development of efficient neuromorphic computing. Here, we experimentally demonstrated an Ga₂O₃-based metal–semiconductor–metal (MSM) solar-blind ultraviolet (UV) photodetector (PD) with asymmetric interdigital electrodes. The Ga₂O₃ PD exhibits a responsivity of 732 A/W under a forward bias of 6 V. The tunable conductance properties of PDs provide a novel approach to synaptic performance. The proposed PDs as artificial synapse realized several essential synaptic function, including excitatory post-synaptic current, paired-pulse facilitation, long-term potentiation, the transition from short-term memory to long-term memory, and learning experience behaviors successfully. At a reverse bias, an ultra-low energy consumption of 140 fJ was achieved. In addition, the optoelectronic synapses demonstrated a recognition accuracy of over 95% in the MNIST handwritten number recognition task. These results suggest that Ga₂O₃ MSM solar-blind UV PDs have high potential for efficient optoelectronic neuromorphic computing applications.

Keywords

asymmetric electrodes, Ga₂O₃, neuromorphic computing, optoelectronic synapse, solar-blind UV PDs

1 | INTRODUCTION

In recent years, optoelectronic devices based on wide-bandgap semiconductor materials have attracted significant attention, particularly for deep-ultraviolet (UV) detection. β -Ga₂O₃, a wide-bandgap oxide semiconductor with outstanding properties, has become a focal point of research. Its wide bandgap of approximately 4.9 eV enables excellent optical response across the UV to visible spectrum. Additionally, its high breakdown electric field strength, thermal stability, and chemical robustness make it highly suitable for applications in high-power electronics, deep-UV photodetectors (PDs), and other optoelectronic

fields.^[1–8] Notably, tuning the optoelectronic properties of β -Ga₂O₃ through defects such as oxygen vacancies has proven highly effective in enhancing device performance. These defects significantly influence the generation, transport, and recombination of carriers, providing theoretical insights for developing high-sensitivity and stable PDs.

As demand for neuromorphic computing grows, research efforts are increasingly exploring the potential of β -Ga₂O₃ in artificial synapse. Artificial synapses, which mimic the learning and memory mechanisms of biological synapses, hold promise for advancing next-generation artificial intelligence hardware.^[9] With its low power consumption, tunable properties, and excellent optical response, β -Ga₂O₃

This is an open access article under the terms of the [Creative Commons Attribution](https://creativecommons.org/licenses/by/4.0/) License, which permits use, distribution and reproduction in any medium, provided the original work is properly cited.

© 2025 The Author(s). *Responsive Materials* published by John Wiley & Sons Australia, Ltd on behalf of Southeast University.

is considered a strong candidate for achieving artificial synaptic functionality.^[10]

Despite substantial progress in the study of PDs and neuromorphic computing, most optoelectronic devices remain constrained by single-function limitations, making it difficult to meet the needs of multifunctional integration. Traditional PDs often require multiple sequential steps to collect, store, and transmit data to neural networks.^[11–17] This approach not only increases energy consumption and computation time but also risks information loss. To address these challenges, researchers have been actively developing devices that integrate photodetection and neuromorphic computing functionalities. For example, Su et al. introduced a self-powered solar-blind UV PD based on a GaSe/Ga₂O₃ heterojunction. This device achieved a responsivity of 1.49 mA/W and a detectivity of 6.65×10^{11} Jones under extremely low light conditions.^[18] Similarly, Yü et al. designed a solar-blind UV PD utilizing AlGaIn and two-dimensional MXene, which demonstrated a responsivity of 3 A/W under 270 nm UV illumination.^[19] While these devices exhibit certain levels of photoresponse, their overall performance remains limited.^[20–22] In the area of functional integration, Feng et al. developed a trench-bridged GaN/Ga₂O₃/GaN back-to-back double heterojunction array device. This system showed rapid photoresponse at low voltages and a persistent photoconductive effect at high voltages. Adjusting the bias voltage allowed switching between photodetection and neuromorphic computing functionalities.^[23] However, these devices often face limitations in photoresponse and insufficient tunability in conductance, creating obstacles to advanced functional integration.^[24–26] Consequently, there is a pressing need to develop high-performance optoelectronic devices capable of seamless functionality switching.^[27–29]

This study explores β -Ga₂O₃ PDs for neuromorphic applications. High-quality Ga₂O₃ thin films were synthesized using metal-organic chemical vapor deposition (MOCVD), and the optimized asymmetric metal electrodes were employed to construct a PD with exceptional performance. The experimental results not only characterized the device's optoelectronic properties but also investigated its ability to mimic synaptic learning and forgetting mechanisms. The device demonstrated key synaptic behaviors such as the transition from short-term memory (STM) to long-term memory (LTM), excitatory postsynaptic current (EPSC), and long-term potentiation (LTP). Furthermore, it achieved high sensitivity, low power consumption, and significant tunability. These findings provide a strong foundation for the development of neuromorphic computing hardware based on β -Ga₂O₃ and offer innovative solutions for energy-efficient PDs.

2 | EXPERIMENTAL SECTION

The stereogram of the fabricated PD is presented in Figure 1a. During device preparation, a Ga₂O₃ film with a thickness of 1075 nm acting as the active layer was initially

grown on a sapphire substrate via MOCVD. A Schottky contact based on Ni/Au (30 nm/150 nm) metal stack was directly on the Ga₂O₃ layer and patterned via e-beam on the lift-off process. Furthermore, Ti/Au (20 nm/80 nm) metal stack was deposited on the Ga₂O₃ layer and was annealed in an N₂ atmosphere at 500°C for 60 s to form an Ohmic contact. As indicated in Figure 1b, the distance between the interdigital electrodes was 10 μ m, the fingers of the electrodes were 400 μ m long with the Schottky contact of 10 μ m wide and the Ohmic contact of 20 μ m wide. It can be observed that the electrode surface is smooth and free from contamination, in the image. Correspondingly, the effective area of the device was 0.072 mm². Upon illumination, the incident light is absorbed in this effective area, resulting in the generation of electron-hole pairs. The bias voltage applied to the electrodes exerts a force on the electron-hole pairs, causing them to drift and be collected, thereby generating a photocurrent.

Atomic force microscopy (AFM) and Raman spectroscopy were used to examine the crystal quality of the samples. A UV-vis spectrophotometer recorded the absorption spectrum of the Ga₂O₃ film. Moreover, to analyze the PD's photoelectric properties, a semiconductor parameter analyzer (Keithley 2636B) measured the current-voltage (*I*–*V*) characteristics both in darkness and under illumination. A 150-W Xenon lamp served as the light source for measuring the device's spectral response. The optical power density corresponding to different wavelengths was calibrated via a standard Si-based PD. Simultaneously, the transient time-dependent light responses were measured. In the artificial synapse mode, the Xenon lamp shutter converted continuous light into pulsed light for the device. The pulsed light modulation was utilized to simulate synaptic behavior, while the current response was recorded using the Keithley 2636B. These measurements are directly related to neuromorphic computing applications, as the current changes reflect synaptic plasticity phenomena. By adjusting optical parameters such as light intensity, pulse width, and frequency, the EPSC of the device can be directly influenced, laying the foundation for simulating synaptic learning and forgetting behaviors.

3 | RESULTS AND DISCUSSION

β -Ga₂O₃ was selected for this study due to the presence of specific defects, particularly oxygen vacancies. The defects impact the synaptic properties of the material. The surface morphology of the Ga₂O₃ epitaxial layer was obtained through AFM. Figure 1c illustrated the 2-D AFM image of the Ga₂O₃ layer within a scanning area of 10 \times 10 μ m². The results of the study show that the surface root mean square roughness is \sim 3.19 nm, indicating that the Ga₂O₃ thin film exhibits an optimal morphology. Raman spectroscopy characterized the molecular features of the Ga₂O₃ layer, as shown in, as depicted in Figure S1. A peak at 200 cm^{–1} closely aligns with the phonon mode at 199 cm^{–1}. Similarly,

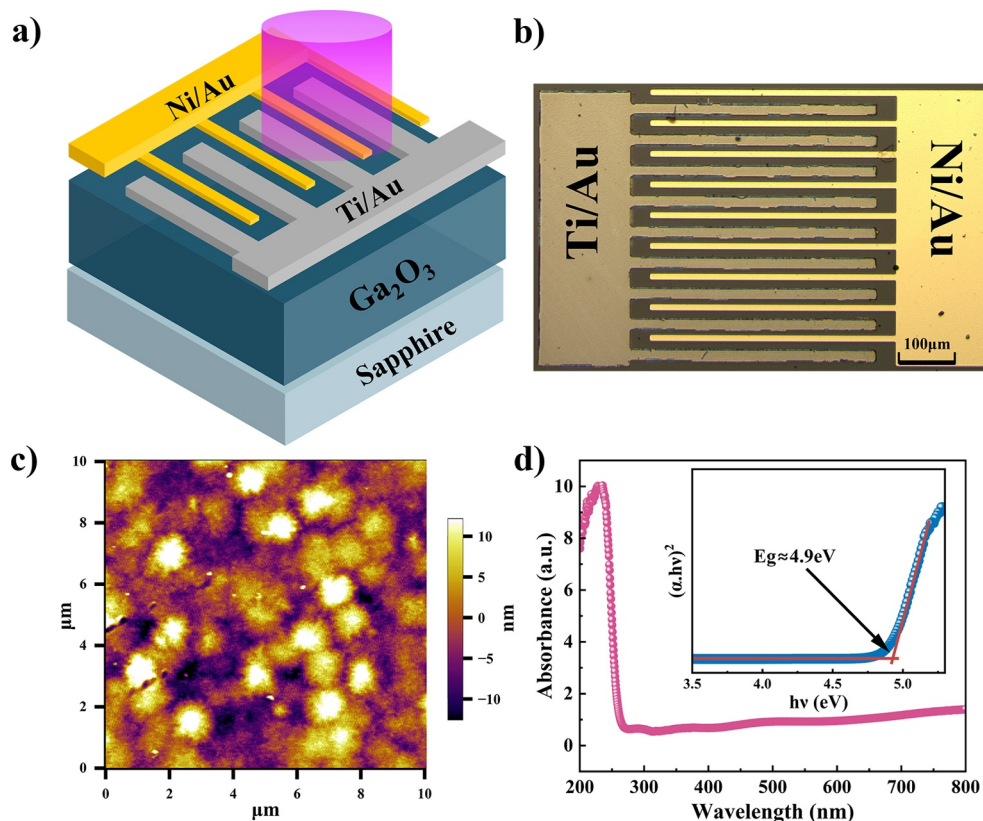


FIGURE 1 (a) Schematic diagram of the ultraviolet (UV) photodetector with asymmetric electrodes. (b) Optical micrograph of the PD. (c) Atomic force microscopy surface morphology of the Ga₂O₃ layer. (d) UV-visible absorption spectrum of the Ga₂O₃ film.

a peak near 400 cm⁻¹ corresponds to the A_{1g} mode at 417 cm⁻¹, and another near 600 cm⁻¹ aligns with the A_{1g} mode at 620 cm⁻¹. These observed peaks confirm the characteristic Raman features of β-Ga₂O₃. Simultaneously, Figure 1d displays the optical absorption characteristics of the Ga₂O₃ layer, measured using a UV-vis spectrometer. The absorption edge shows a steep cutoff around 250 nm, with strong absorption in the solar-blind region. In addition, extrapolating the (αhν)² curve as a function of photon energy (hν) reveals a Ga₂O₃ bandgap of approximately 4.9 eV, as shown in the inset of Figure 1d.^[30] Oxygen vacancies and other defects in Ga₂O₃ contribute to an increase in absorption beyond 250 nm.

Figure 2a presents the photodetection performance of the metal–semiconductor–metal PD with asymmetric contact electrodes. *I*–*V* measurements were conducted with a –6 to 6 V voltage sweep across the electrodes, both in the dark and under 250 nm UV illumination. Under an incident optical power density of 22 μW/cm², the device demonstrates a significant response current at both reverse and forward bias voltages. At –6 V, the dark current is as low as 6.78 × 10⁻¹² A, with a corresponding photocurrent of 2.4 × 10⁻⁹ A. At 6 V, the photocurrent increases to 1.8 × 10⁻⁶ A, while the dark current reaches 2.04 × 10⁻⁸ A. The asymmetrical *I*–*V* curves exhibit rectification characteristics due to the asymmetric contact electrodes. As illustrated in Figure 2b, calibrated spectral response curves were obtained under forward

bias voltages when varying the wavelength from 220 to 350 nm. The results indicate that the PD exhibits a distinct cutoff edge at 270 nm across various bias voltages, aligning with the Ga₂O₃ bandgap. The device exhibits a peak response around 250 nm, unaffected by the polarity of the applied bias. Additionally, the responsivity progressively increases as the bias voltage is raised from 1 to 6 V. Importantly, under a 6 V bias, the peak responsivity reaches an impressive 732 A/W. In addition, the designed device demonstrates a solid response under reverse bias conditions, as shown in Figure S2a, with a peak responsivity of 0.35 A/W. It is worth mentioning that the peak responsivities are relatively higher under forward bias than under reverse bias; for instance, at 6 V forward bias, the responsivity reaches its maximum, whereas it is 0.35 A/W at –1 V reverse bias. Figure 2c and Figure S2b present the time-dependent current (*I*–*T*) curves obtained under periodic ON/OFF switching of the Xenon lamp with both forward and reverse bias voltages, recorded over 40-s intervals. The data demonstrates a clear increase in current with the light on and a decrease with it off, indicating robust switching performance. The device exhibits excellent stability and consistent reproducibility across different bias polarities.^[31]

The designed device is capable of performing various neural synapse functions. Figure 3a presents the synapse as a specific connection point between neurons, serving as the fundamental structural unit for signal transmission within the

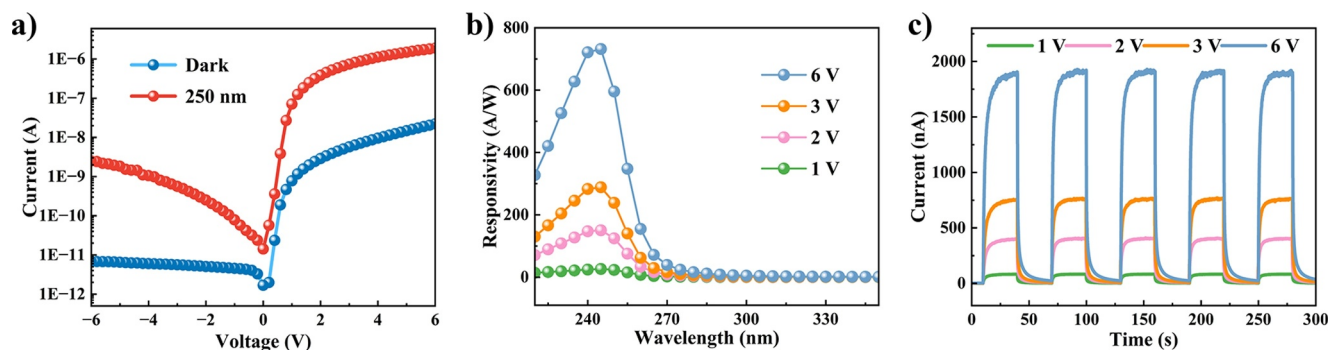


FIGURE 2 (a) The I - V characteristics of the photodetector (PD) under dark conditions and 250 nm illumination. (b) Spectral responsivities of the device at applied biases ranging from 1 to 6 V. (c) Time-dependent photocurrent responses of the PD under forward voltages.

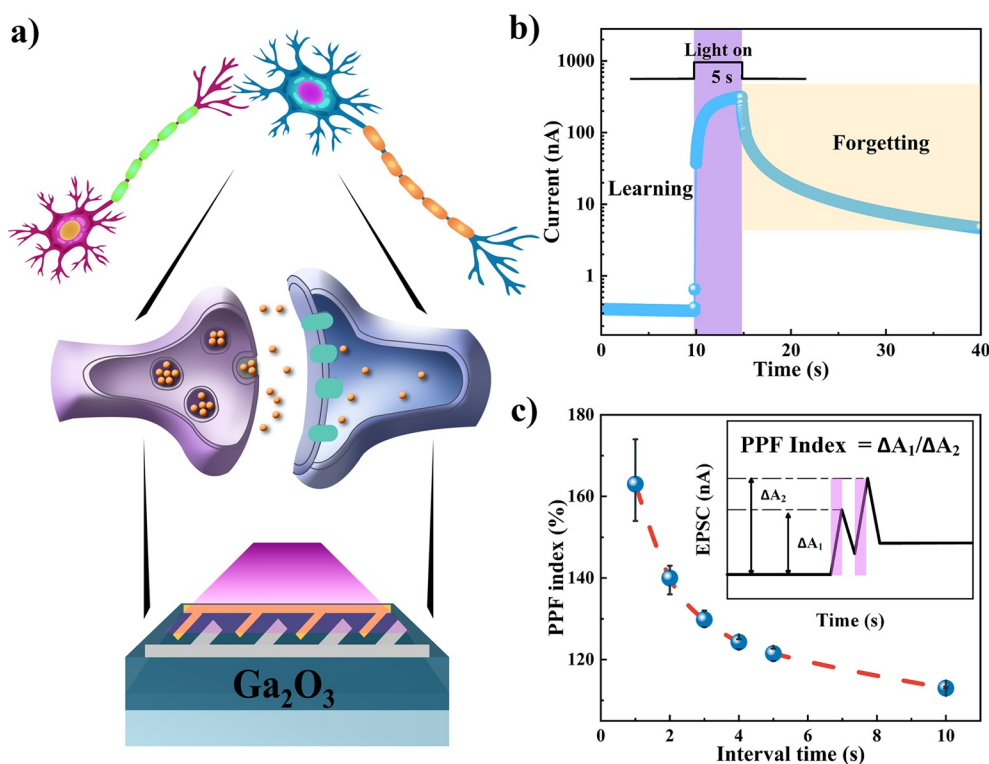


FIGURE 3 (a) Schematic diagram of synaptic structures. (b) Overview of the “learning” and “forgetting” processes in synaptic structures. (c) Effect of light pulse stimulation time intervals on the paired-pulse facilitation (PPF) effect.

nervous system. The synapse comprises a presynaptic membrane, a synaptic cleft, and a postsynaptic membrane.^[32] Upon generation of an action potential by the presynaptic neuron, calcium ion channels on the presynaptic membrane open, leading to the fusion of synaptic vesicles containing neurotransmitters with the presynaptic membrane. This process results in the release of neurotransmitters into the synaptic cleft, allowing them to diffuse toward the postsynaptic membrane and bind to receptors there, ultimately triggering an action potential in the postsynaptic neuron. Changes in postsynaptic potentials can be categorized as excitatory postsynaptic potentials (EPSPs) or inhibitory postsynaptic potentials (IPSPs). EPSPs facilitate

the generation of action potentials in the postsynaptic neuron, whereas IPSPs inhibit this process.^[33–35]

Synaptic plasticity describes the ability of neural activity to modify the strength of synaptic connections, forming a crucial basis for learning and memory within the nervous system. This plasticity is categorized into two distinct types based on the duration of its effects: long-term synaptic plasticity and short-term synaptic plasticity. LTP denotes a sustained increase or decrease in synaptic strength, typically associated with LTM, lasting from minutes to decades. In contrast, short-term plasticity (STP) signifies a temporary alteration in synaptic strength, often linked to STM, with durations generally ranging from seconds to minutes. While

STM and LTM serve different roles in the memory system, mechanisms exist for their conversion. For instance, under certain conditions, STM can transition into LTM through enhanced synaptic plasticity, often necessitating repeated or reinforced stimulation to facilitate memory consolidation. The dynamic modulation of synaptic transmission efficiency not only influences the signaling of individual synapses but also contributes to the adaptability of neural networks.

The artificial synapse resembles a biological synapse, featuring a gap between the interdigital electrodes. Figure 3b depicts the temporal evolution of the device's current in response to a 2 V bias voltage applied at both ends and the subsequent exposure to 250 nm UV light for a duration of 5 s. As illustrated in the figure, the onset of light stimulation is accompanied by a rapid increase in current, indicative of the device's transition into the "learning" stage.^[36] Over the following 5 s, despite continuous illumination, the current increase slows and reaches a peak value, signaling the completion of the learning process. After the light stimulation ends, the current does not instantly revert to its initial value but instead decreases gradually at a slower rate. This process represents the forgetting process of the synapse. The current then returns to its baseline level, signaling the completion of the forgetting process. This behavior mirrors the learning and forgetting mechanisms observed in neural synapses, as discussed earlier. Adjustments to the artificial synapse's learning and forgetting processes can be achieved by modifying light stimulation parameters, such as light power intensity, pulse count, pulse frequency, and pulse width. The capacity to regulate device functionality presents a promising path for emulating the operations of biological synapses. This capability may contribute to deeper insights into neuromorphic computing and drive advancements in artificial intelligence hardware.^[37]

Figure 3c illustrates the influence of the time interval of light pulse stimulation on the paired-pulse facilitation (PPF) effect, with the inset showing the PPF effect of the detector. The image illustrates the experimental outcomes of applying a 2 V bias voltage to both ends of the artificial synapse and administering two consecutive pulses of stimulation using 250 nm UV light. In this experiment, each light pulse has a duration of 1 s, with an interval of 2 s between pulses. The inset of Figure 3c illustrates that the current amplitude generated by the initial light pulse is labeled as A_1 , while the amplitude generated by the subsequent light pulse is labeled as A_2 . Here, ΔA_1 and ΔA_2 represent the differences between the current induced by the first and second light pulses and the baseline dark current. PPF is typically employed to describe the augmentation of the amplitude of the EPSC in response to two successive pulse stimulations.^[38] The PPF index calculation follows the formula: $\text{PPF index} = (\Delta A_2 / \Delta A_1) \times 100\%$. To further quantify the PPF effect, we examined the PPF index across varying pulse time intervals (Δt). The figure illustrates EPSC behavior triggered by two optical pulses with a fixed interval. The EPSC amplitude A_2 generated by the second light pulse significantly surpasses that of the first pulse, with a nearly 1.65 fold increase. This enhancement arises from an elevated number of captured

electrons in the device at the time of the second pulse, producing a higher current. The subsequent accumulation of photogenerated carriers amplifies the PPF effect. This observed behavior mirrors the mechanism in biological synapses, where the PPF effect similarly relies on the interval between pulses. The increase in amplitude highlights the device's capacity for synaptic-like responses, reinforcing its potential for neuromorphic applications. Additionally, Figure 3c demonstrates that the PPF index steadily decreased as the interval between pulses increased from 1 to 10 s. This diminishing trend can be effectively represented by the following double exponential function, resembling the dynamics observed in biological synapses.

$$\text{PPF} = 1 + C_1 \exp\left(\frac{-\Delta t}{\tau_1}\right) + C_2 \exp\left(\frac{-\Delta t}{\tau_2}\right) \quad (1)$$

In this function, Δt denotes the time interval between light pulses, while C_1 and C_2 represent the initial magnitudes of facilitation. Additionally, τ_1 and τ_2 indicate the characteristic relaxation times for the rapid and slow decay phases, respectively.^[39] τ_1 primarily reflects the rapid recombination dynamics of free carriers, influenced by carrier mobility and shallow trap density. τ_2 is determined by the trapping and release mechanisms in deep-level traps, significantly affected by the density and distribution of oxygen traps. Δt plays a key role in regulating carrier generation and recombination rates, thereby impacting τ_1 and τ_2 . Consequently, the values obtained for C_1 , C_2 , τ_1 , and τ_2 were 88.06, 127.23, 1.13, and 78.35 s, respectively. Notably, τ_1 is an order of magnitude smaller than τ_2 , reflecting a similarity to the decay dynamics observed in biological synapses.

The learning and forgetting processes of the artificial synapse can be regulated by adjusting the parameters of light stimulation, including light power, pulse count and frequency, and pulse width. Figure 4a illustrates the post-synaptic current (PSC) responses under three different power conditions with a pulse width of 500 ms. PSC, defined as the device's current that gradually decreases from peak photocurrent to dark current after light stimulation, directly influences synaptic performance. Tests were conducted at power levels of 1, 5, and 10 $\mu\text{W}/\text{cm}^2$. Enhanced light intensity led to more pronounced synaptic responses, evident in the increased spike currents and prolonged relaxation times. This observation suggests that higher power levels contribute to prolonged memory retention. Figure 4b examines the effects of varying single pulse durations on the synaptic performance of the device. Under a 2 V bias with 250 nm UV light, PSC was evaluated across pulse durations of 1, 2, 3, 5, 10, 20, and 50 s. The findings reveal that prolonged light stimulation time gradually enhances PSC, indicating greater synaptic plasticity. Figure 4c presents the PSC responses obtained by continuously applying 1, 2, 3, and 5 pulses of 250 nm light with a pulse width of 500 ms and an interval of 500 ms. The inset depicts the response under 30 consecutive light pulses. It is evident that each subsequent pulse amplifies the response elicited by the preceding pulse. Although the overall enhancement trend

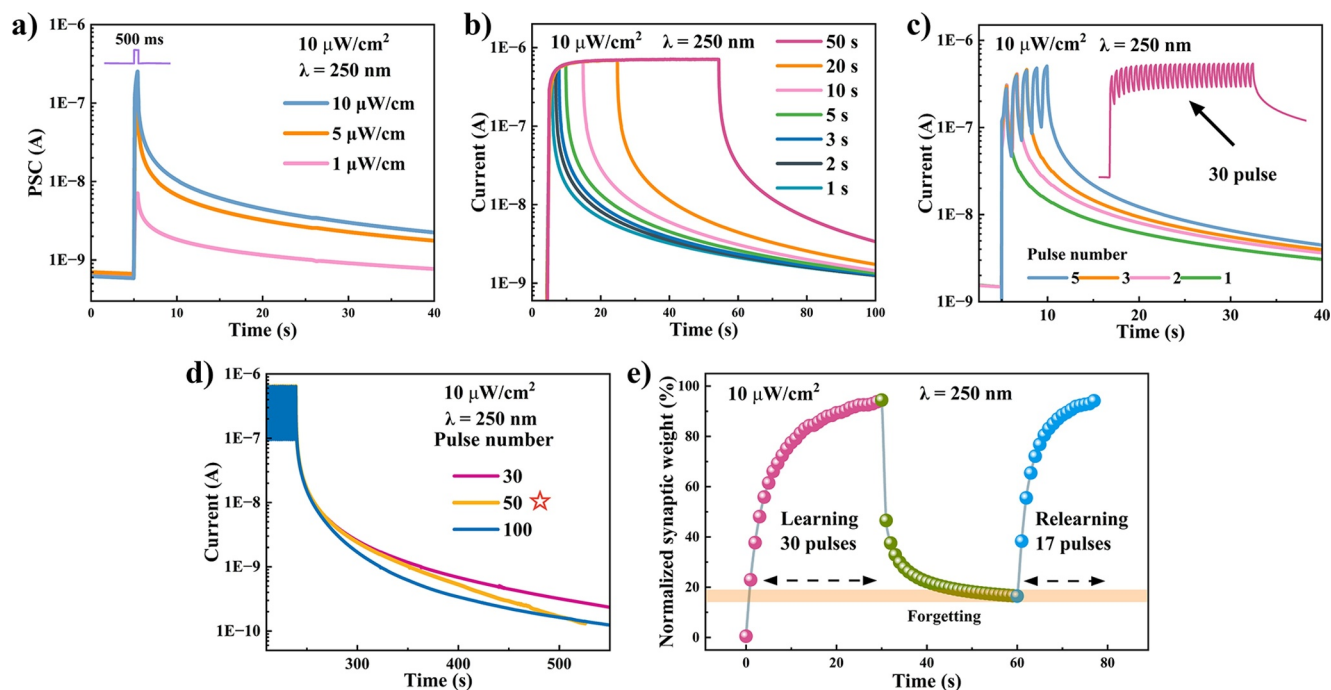


FIGURE 4 (a) Postsynaptic current (PSC) at light intensities of 1, 5, and $10\text{ }\mu\text{W}/\text{cm}^2$ with a 500 ms pulse width under a 2 V bias. (b) PSC response under a 2 V bias with single pulse durations of 1, 2, 3, 5, 10, 20, and 50 s. (c) PSC variation with 1, 2, 3, 5, and 30 consecutive 250 nm light pulses at 500 ms pulse width and 500 ms interval. (d) PSC changes with 30, 50, and 100 consecutive 250 nm light pulses, each with 500 ms width and interval. (e) "Learning-experience" behavior of the artificial synapse, including learning, forgetting, and relearning processes.

persists with increasing pulse counts, the magnitude of enhancement from subsequent pulses diminishes, as indicated in the inset and Figure 4d. Notably, as the number of consecutive light pulses increases from 30 to around 100, a transition occurs from LTM to STM. Appropriate adjustments to light stimulation can facilitate the conversion of STM into LTM in this artificial synapse.^[40–42]

Additionally, the artificial synapse demonstrated low-power characteristics under a reverse bias condition of -2 V , as shown in Figure S4. Under these conditions, the device exhibited a maximum EPSC of 70 pA and demonstrated the capability to transition from STP to LTP through modulation of light stimulation. The energy consumption (E) is calculated using the formula $E = I_{\text{peak}} \times V \times T_d$, where I_{peak} represents the maximum EPSC, V is the bias voltage, and T_d is the pulse duration. The synapse demonstrates an energy consumption of 140,000 fJ. By further reducing the bias voltage and the duration of light stimulation, the energy consumption can be lowered to 140 fJ, reaching the scale of biological synapses. The research on low-power optoelectronic synapses provides a crucial energy solution for neuromorphic computing, driving the development of energy-efficient synaptic devices in the field of artificial intelligence hardware.

Furthermore, the repeatable plasticity of biological synapses enables the human brain to undergo a learn-forget-relearn cycle when acquiring new knowledge. This relearning phase requires significantly less time to recall the same information compared to the initial learning phase. Figure 4e illustrates this "learning experience" by

stimulating the artificial synapse with a series of 30 consecutive light pulses. Under this optical stimulation, the PSC shows a sustained increase. Following the stimulation of the light pulses, the PSC begins to decline, corresponding to the forgetting phase in the learning process. Additional light pulses are applied to the device to recover the forgotten information. Remarkably, the artificial synapse requires only 17 optical pulses to reach the previous learning level, a significant reduction compared to the initial learning phase.

The weights of optoelectronic artificial synapses can be modified by external factors, such as the frequency and duration of light stimulation. The designed artificial synapse features a bidirectional structure. In addition to light enhancement, applying reverse bias voltage pulses effectively eliminates the PSC signal, thereby achieving electrical suppression and ensuring the device's capacity for repeated operations. Figure S4 illustrates the normalized conductance changes of the artificial synapse over time (seconds), reflecting its behavior during both growth and decay cycles. The conductance increase phase represents the device's response to external stimuli, with gradual accumulation over time. Conversely, the decay process corresponds to a reduction in conductance, gradually returning to a lower initial level. These measurements are presented in the form of a weight matrix, simulating the connection strengths between neurons.

Comprehensive validation of the feasibility of utilizing these devices within neural networks was conducted, alongside an in-depth investigation of their effects on enhancing plasticity. The conductance values obtained from the devices served as the initial weights for the matrix

between the input layer and hidden layer. This conductance matrix functioned as the initial weight matrix for the neural network, which was employed to classify and recognize the MNIST handwritten digit dataset. The proposed fully connected neural network architecture is illustrated in Figure 5a, featuring an input layer comprising 784 nodes corresponding to the 28×28 pixel MNIST dataset. The processing layer contains two hidden layers with 128 and 64 nodes, respectively, while the output layer consists of 10 nodes representing the classifications from digit 0 to 9. The figure demonstrates the feature extraction process for input images (e.g., “6”) across various layers, highlighting how feature representation evolves with layer depth. The connection weights between nodes are simulated based on the conductance values of the devices, which can change under light exposure, thus reflecting the plasticity of the optoelectronic artificial synapse. This adaptability enhances the artificial synapse's flexibility, allowing for repeated use during the training of the neural network.

Figure 5b presents the variations in accuracy and loss throughout the training process. During the initial training stages, accuracy rises rapidly while loss decreases sharply, indicating that the network effectively learns and adapts to the data.^[43] In the first five iterations, the classification

accuracy reaches approximately 95%. After 20 iterations, the loss stabilizes, and accuracy hovers around 97% following 50 iterations. These results demonstrate the neural network's strong learning capability and high convergence speed, attributable to the adjustable nature of the device's weight matrix and its robustness.

To further evaluate classification performance, a confusion matrix was analyzed, as depicted in Figure 5c. This matrix provides a detailed account of the model's classification effectiveness, comparing predicted labels (rows) with true labels (columns) to assess recognition accuracy for each digit. Higher values along the diagonal (highlighted in green) indicate correct classifications, while values off the diagonal reveal misclassifications, exposing digits that the model finds difficult to distinguish. For instance, the digit “1” exhibits a low misclassification rate with minimal errors. The findings indicate that the artificial synapse achieves very low recognition errors, showcasing excellent classification performance. The design of the asymmetric interdigital electrode enables effective perception and memory operations under UV illumination, enhancing the artificial synapse's potential applications in image recognition.^[44]

Figure 6 outlines the mechanism of non-equilibrium carrier generation, capture, and release (de-capture) in

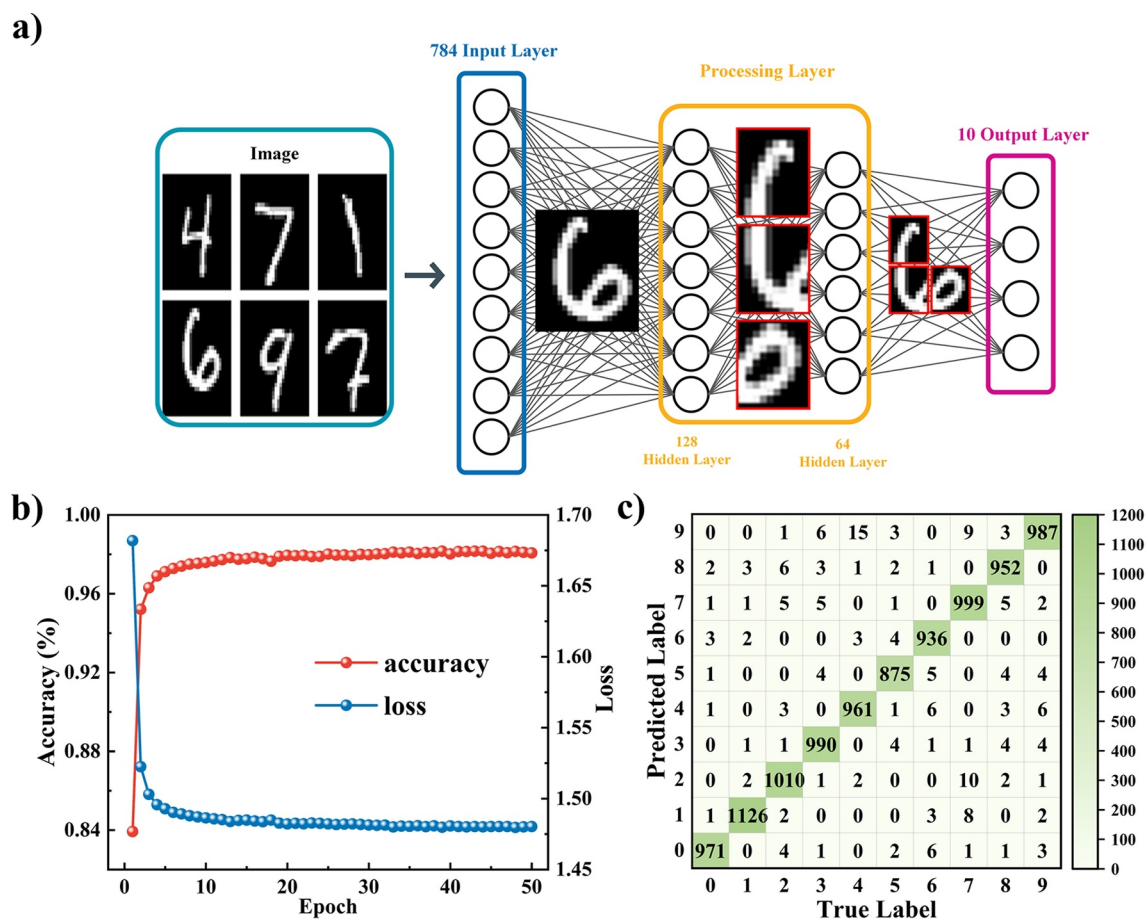


FIGURE 5 (a) Structure of the designed fully connected neural network. (b) Accuracy and loss curves over 50 iterations. (c) Confusion matrix of the artificial synapse for MNIST recognition tasks.

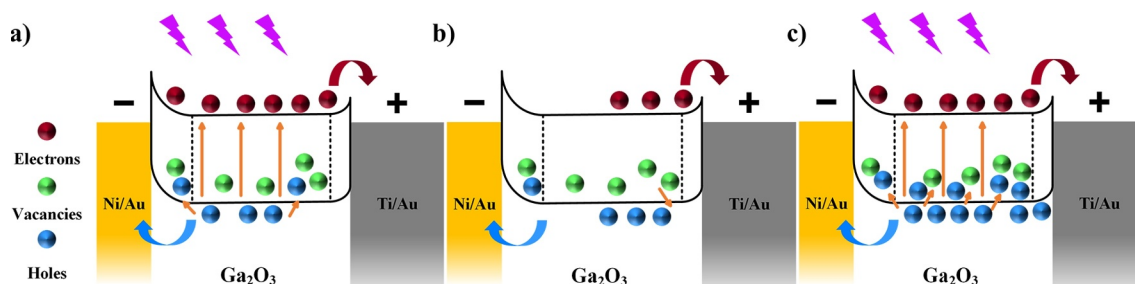


FIGURE 6 (a) Stage 1—light application. (b) Stage 2—light source removal. (c) Stage 3—reapplication of light.

Ga₂O₃ thin-film devices. The device's detection mode operates in three primary phases: accumulation under illumination, exhaustion after illumination stops, and re-excitation upon re-illumination. To clarify the PPF effect, we present the UV PD's band structure in various states. Before the first stage, with no illumination, thermal excitation generates background carriers in Ga₂O₃'s conduction band from shallow energy-level defects, contributing to the device's dark current. During the accumulation phase, with a 2 V bias applied and exposure to 250 nm deep UV light, the PD switches to accumulation mode. Figure 6a shows increased electron transitions, occurring both between the conduction and valence bands and through sub-bandgap levels associated with oxygen defects. This rapid increase in electron-hole pairs within the active layer results in substantial carrier accumulation. The applied bias drives this buildup, significantly boosting photocurrent and enhancing device responsiveness. The applied bias drives this buildup, significantly boosting photocurrent and enhancing device responsiveness. Meanwhile, holes move toward the Ga₂O₃ Ni/Au electrode interface, where oxygen vacancies and other defects capture them. The strong capture capability of deep-level defects, including oxygen vacancies, produces the persistent photoconductivity (PPC) effect, with research indicating that long-term hole capture predominantly underlies the PPC effect in Ga₂O₃ thin films.^[45] In the exhaustion phase, shown in Figure 6b after illumination ceases, an energy barrier within the device extends the photocurrent decay period. An indirect recombination center at this stage regulates decay rate, as the gradual release and recombination of trapped holes with electrons leads to sustained photocurrent. In the re-excitation phase, illustrated in Figure 6c, trapped holes contribute to an increase in free electron concentration, initiating the PPF effect. Upon re-illumination, the release and recombination of these trapped holes with incoming electrons raise the photocurrent once again, resulting in a distinct PPF effect in the device.

4 | CONCLUSION

In conclusion, this work demonstrates the design and fabrication of a PD based on β -Ga₂O₃ thin films, highlighting its outstanding performance in solar-blind UV photodetection

and artificial synapse applications. By employing an asymmetric metal electrode configuration, the device exhibits superior optoelectronic properties under both forward and reverse bias, including high photoresponsivity, low dark current, and stable switching behavior. Moreover, the PD successfully emulates biological synaptic behaviors, such as learning and forgetting, by modulating optical stimulation parameters like intensity, pulse number, and duration. It achieves both short-term and long-term plasticity, as well as a pronounced PPF effect, presenting significant potential for neuromorphic computing. The device's conductance matrix was further applied in neural network training, effectively enhancing the accuracy of MNIST handwritten digit recognition. Overall, this research provides a foundation for the development of low-power, tunable optoelectronic synaptic devices and offers critical technological support for next-generation artificial intelligence hardware and neuromorphic computing systems.

AUTHOR CONTRIBUTIONS

Huazhen Sun: Investigation; writing—original draft; writing—review & editing; methodology; formal analysis; data curation. **Bingjie Ye:** Investigation; formal analysis. **Mei Ge:** Investigation; formal analysis. **Biao Gong:** Investigation; formal analysis. **Leyang Qian:** Investigation; formal analysis. **Irina N. Parkhomenko:** Formal analysis; data curation. **Fadei F. Komarov:** Data curation; formal analysis. **Yu Liu:** Formal analysis. **Guofeng Yang:** Conceptualization; methodology; data curation; supervision; writing—review & editing.

ACKNOWLEDGMENTS

This work was funded by the National Natural Science Foundation of China (No. 62374075, 61974056, 62375028), the Key Research and Development Program of Jiangsu Province (No. BE2020756), and the Research and Practice Projects on Postgraduate Education and Teaching Reform of Jiangnan University (YJSJGZD24_006).

CONFLICT OF INTEREST STATEMENT

The authors declare no conflict of interest.

DATA AVAILABILITY STATEMENT

The data that support the findings of this study are available from the corresponding authors upon reasonable request.

ORCID

Guofeng Yang  <https://orcid.org/0000-0002-4409-9685>

REFERENCES

1. K. J. Lee, R. Wei, Y. Wang, J. Zhang, W. Kong, S. K. Chamoli, T. Huang, W. Yu, M. Elkabbash, C. Guo, *Nat. Photonics* **2023**, *17*, 236.
2. F. Wang, T. Zhang, R. Xie, A. Liu, F. Dai, Y. Chen, T. Xu, H. Wang, Z. Wang, L. Liao, J. Wang, P. Zhou, W. Hu, *Adv. Mater.* **2023**, 2301197.
3. Y. Zhang, W. Shen, S. Wu, W. Tang, Y. Shu, K. Ma, B. Zhang, P. Zhou, S. Wang, *ACS Nano* **2022**, *16*, 19187.
4. N. F. Yan, H. M. Cui, J. S. Shi, S. Y. You, S. Liu, *Tungsten* **2023**, *5*, 371.
5. M. Dai, H. Chen, F. Wang, Y. Hu, S. Wei, J. Zhang, Z. Wang, T. Zhai, P. Hu, *ACS Nano* **2019**, *13*, 7291.
6. J. Wang, C. Chu, K. Tian, J. Che, H. Shao, Y. Zhang, K. Jiang, Z.-H. Zhang, X. Sun, D. Li, *Photonics Res.* **2021**, *9*, 734.
7. K. S. Pasupuleti, S. S. Chougule, N. Jung, Y. J. Yu, J. E. Oh, M. D. Kim, *Appl. Surf. Sci.* **2022**, *594*, 153474.
8. K. S. Pasupuleti, M. Reddeppa, B. G. Park, K. R. Peta, J. E. Oh, S. G. Kim, M. D. Kim, *ACS Appl. Mater. Interfaces* **2020**, *12*, 54181.
9. B. J. Shastri, A. N. Tait, T. Ferreira de Lima, W. H. P. Pernice, H. Bhaskaran, C. D. Wright, P. R. Prucnal, *Nat. Photonics* **2021**, *15*, 102.
10. P. Monalisha, A. P. S. Kumar, X. R. Wang, S. N. Piramanayagam, *ACS Appl. Mater. Interfaces* **2022**, *14*, 11864.
11. D. G. Roe, D. H. Ho, Y. Y. Choi, Y. J. Choi, S. Kim, S. B. Jo, M. S. Kang, J. H. Ahn, J. H. Cho, *Nat. Commun.* **2023**, *14*, 5.
12. P. Monalisha, S. Li, T. Jin, P. S. A. Kumar, S. N. Piramanayagam, *J. Phys. D Appl. Phys.* **2023**, *56*, 015302.
13. H. Shi, B. Wang, X. Wang, L. Qiu, L. Zheng, *ACS Appl. Mater. Interfaces* **2023**, *15*, 9705.
14. K. T. Chen, L. C. Shih, S. C. Mao, J. S. Chen, *ACS Appl. Mater. Interfaces* **2023**, *15*, 9593.
15. A. Saleem, D. Kumar, F. Wu, L. B. Keong, T. Y. Tseng, *IEEE Trans. Electron Devices* **2023**, *70*, 1351.
16. M. M. Mburu, K. T. Lu, N. L. Prine, A. N. Au-Duong, W. H. Chiang, X. Gu, Y. C. Chiu, *Adv. Mater. Technol.* **2022**, *7*, 2101506.
17. X. Chen, Y. Xue, Y. Sun, J. Shen, S. Song, M. Zhu, Z. Song, P. Zhou, *Adv. Mater.* **2022**, *35*, 2203909.
18. S. Ran, X. Zhao-Ying, L. Shan, Z. Jia-Han, M.-M. J. Zeng, W.-H. Tang, *Acta Phys. Sin.* **2024**, *73*, 118502.
19. J. Z. Yü, Y. Q. Zhang, L. Y. Wang, X. J. Yang, Y. Yang, K. Jiang, W. Lü, X. J. Sun, *Ionics* **2024**, *30*, 1785.
20. T. He, H. Ma, Z. Wang, Q. Li, S. N. Liu, S. K. Duan, T. F. Xu, J. C. Wang, H. T. Wu, F. Zhong, Y. T. Ye, J. H. Wu, S. Lin, K. Zhang, P. Martyniuk, A. Rogalski, P. Wang, L. Li, H. T. Lin, W. D. Hu, *Nat. Photonics* **2024**, *18*, 60.
21. D. H. Wang, W. T. Wu, S. Fang, Y. Kang, X. N. Wang, W. Hu, H. B. Yu, H. C. Zhang, X. Liu, Y. M. Luo, J. H. He, L. Fu, S. B. Long, S. Liu, H. Sun, *Light Sci. Appl.* **2022**, *11*, 227.
22. H. C. Zhang, F. Z. Liang, K. Song, C. Xing, D. H. Wang, H. B. Yu, C. Huang, Y. Sun, L. Yang, X. L. Zhao, H. D. Sun, S. B. Long, *Appl. Phys. Lett.* **2021**, *118*, 242105.
23. S. Feng, J. Li, L. Feng, Z. Liu, J. Wang, C. Cui, O. Zhou, L. Deng, H. Xu, B. Leng, X. Chen, X. Jiang, B. Liu, X. Zhang, *Adv. Mater.* **2023**, *35*, 49.
24. S. Ge, F. Huang, J. He, Z. Xu, Z. Sun, X. Han, C. Wang, L. Huang, C. Pan, *Adv. Opt. Mater.* **2022**, *10*, 11.
25. Z. Wang, G. Zhang, X. Zhang, C. Wu, Z. Xia, H. Hu, F. Wu, D. Guo, S. Wang, *Adv. Opt. Mater.* **2024**, *12*, 2401256.
26. L. Zheng, R. Zhou, S. Xin, H. Cong, Y. Qin, P. Xu, X. Liu, F. Wang, *J. Mater. Chem. C* **2023**, *11*, 7098.
27. Y. Mi, C. Yang, L. Shih, J. Chen, *Adv. Opt. Mater.* **2023**, *11*, 14.
28. B. Bae, M. Park, D. Lee, I. Sim, K. Lee, *Adv. Opt. Mater.* **2022**, *11*, 3.
29. Y. Hou, Y. Li, Z. Zhang, J. Li, D. Qi, X. Chen, J. Wang, B. Yao, M. Yu, T. Lu, *ACS Nano* **2020**, *15*, 1497.
30. D. H. Wang, W. T. Wu, S. Fang, Y. Kang, X. N. Wang, W. Hu, H. B. Yu, H. C. Zhang, X. Liu, Y. M. Luo, J. H. He, L. Fu, S. B. Long, *Nat. Electron.* **2021**, *4*, 645.
31. H. M. Muhammad, H. B. Yu, Y. M. Luo, K. Yang, C. Wei, D. Li, D. Y. Luo, S. D. Xiao, C. J. Zuo, C. Gong, C. Shen, L. Fu, B. S. Ooi, S. Liu, H. Sun, *Nat. Electron.* **2024**, *7*, 279.
32. R. Zhu, H. Liang, S. Hu, Y. Wang, Z. Mei, *Adv. Electron. Mater.* **2021**, *8*, 1.
33. A. Bazzari, H. Parri, *Brain Sci.* **2019**, *9*, 300.
34. M. H. Hennig, *Front. Comput. Neurosci.* **2013**, *7*, 154.
35. S. Li, J. Li, K. Zhou, Y. Yan, G. Ding, S. Han, Y. Zhou, *J. Phys. Mater.* **2024**, *7*, 3.
36. J. Tang, C. He, J. Tang, K. Yue, Q. Zhang, Y. Liu, Q. Wang, S. Wang, N. Li, C. Shen, Y. Zhao, J. Liu, J. Yuan, Z. Wei, J. Li, K. Watanabe, T. Taniguchi, D. Shang, W. Yang, R. Yang, D. Shi, G. Zhang, *Adv. Funct. Mater.* **2021**, *31*, 27.
37. X. Zhu, D. Li, X. Liang, W. D. Lu, *Nat. Mater.* **2018**, *18*, 141.
38. J. An, N. Zhang, F. Tan, X. Zhao, C. Chang, M. Lanza, S. Li, *Small* **2024**, *20*, 2403103.
39. Y. Chen, Y. Huang, J. Zeng, Y. Kang, Y. Tan, X. Xie, B. Wei, C. Li, L. Fang, T. Jiang, *ACS Appl. Mater. Interfaces* **2023**, *15*, 58631.
40. L. Wang, H. Wang, J. Liu, Y. Wang, H. Shao, W. Li, M. Yi, H. Ling, L. Xie, W. Huang, *Adv. Mater.* **2024**, *36*, 2403538.
41. W. Wang, Y. Wang, F. Yin, H. Niu, Y. Shin, Y. Li, E. Kim, N. Kim, *Nano-Micro Lett.* **2024**, *16*, 1.
42. D. Hao, Z. Yang, J. Huang, F. Shan, *Adv. Funct. Mater.* **2022**, *33*, 8.
43. H. C. Zhang, F. Z. Liang, L. Yang, Z. X. Gao, K. Liang, S. Liu, Y. K. Ye, H. B. Yu, W. Chen, Y. Kang, *Adv. Mater.* **2024**, *36*, 2405874.
44. X. Fu, T. X. Li, B. Cai, J. S. Miao, G. N. Panin, X. Y. Ma, J. J. Wang, X. Y. Jiang, Q. Li, Y. Dong, C. H. Hao, J. Y. Sun, H. Y. Xu, Q. X. Zhao, M. J. Xia, B. Song, F. S. Chen, X. S. Chen, W. Lu, W. D. Hu, *Light Sci. Appl.* **2023**, *12*, 39.
45. R. Zhu, H. Liang, H. Bai, T. Zhu, Z. Mei, *Appl. Mater. Today* **2022**, *29*, 101556.

SUPPORTING INFORMATION

Additional supporting information can be found online in the Supporting Information section at the end of this article.

How to cite this article: H. Sun, B. Ye, M. Ge, B. Gong, L. Qian, I. N. Parkhomenko, F. F. Komarov, Y. Liu, G. Yang, *Responsive Mater.* **2025**, *3*, e20240038. <https://doi.org/10.1002/rpm.20240038>